

**On the Profiles and the Polarization of
Raman Scattered Emission Lines in Symbiotic Stars
II. Numerical Simulations**

K. W. Lee¹ & Hee-Won Lee²

¹Dept. of Astronomy and Atmospheric Sciences
Kyungpook National University, Taegu, Korea

² Research Institute for Basic Sciences and Dept. of Astronomy
Seoul National University, Seoul, Korea

email: hwlee@astro.snu.ac.kr

ABSTRACT

A Monte Carlo method is used to calculate the profiles and the polarization of the Raman scattered O VI lines ($\lambda\lambda 6827, 7088$) in symbiotic stars, which are believed to be a binary system of a cool giant and a hot star with an emission nebula around it. A point-like isotropic UV radiation source is assumed and a simple spherical wind model is adopted for the kinematics of the scattering material from the cool giant.

We first investigate the case where the incident line photons are described by a Gaussian profile having a width of 10^4 K. We subsequently investigate the effects of the extended ionized region and non-spherical wind models including a disk-type wind and a bipolar wind. The cases where the emission source is described by non-Gaussian profiles are briefly studied.

Finally as an additional component for the kinematics of symbiotic stars the orbital motion of the hot component around the cool giant is included and the effect on the spectropolarimetry is investigated. In this case the polarization direction changes around the red part of the Raman-scattered emission lines, when the observer's line of sight is perpendicular to the orbital plane, and no such effect is seen when the line of sight lies in the orbital plane. Furthermore, complex peak structures are seen in the degree of polarization and the polarized flux, which have often been observed in several symbiotic systems including RR Tel.

Brief observational consequences and predictions are discussed in relation to the present and future spectropolarimetry for symbiotic stars. It is concluded that spectropolarimetry may provide a powerful diagnostic of the physical conditions of symbiotic stars.

1. Introduction

A symbiotic star is believed to be a binary system consisting of a cool giant and a hot star providing H-ionizing photons for an emission nebula around it (Iben & Tutukov 1996). It is expected that the hot component is characterized by a typical temperature $T \sim 10^{4-5}$ K and that the binary motion has a typical period of $P \sim 10^{2-3}$ days.

The observed spectral parts of the emission in the symbiotic systems cover a very large range including radio, IR, optical, UV and X-rays. The complicated profiles and the significant variabilities often seen in the UV emission lines imply that the dynamics and the physical conditions are not simple enough to be described by a unique model (*e.g.* Vogel & Nussbaumer 1994).

It has been known that a significant fraction of symbiotic stars exhibit broad emission features around $\lambda 6827$ and $\lambda 7088$ with widths up to 20 \AA , which are an order of magnitude larger than those of other emission lines in their typical spectra (*e.g.* Allen 1980). These broad features are identified by H. Schmid (1989) as the Raman scattered O VI $\lambda\lambda 1032, 1038$ by hydrogen atoms. During the scattering process, the atom in the ground state absorbs the incident line photon with frequency ν_i to be excited to an intermediate state followed by de-excitation to the $2s$ state emitting a photon with frequency $\nu_f = \nu_i - \nu_\alpha$, where ν_α is the frequency of the Ly α transition.

The Raman scattering nature explains the large width of the features and many observational characteristics of symbiotic stars such as the existence of highly ionized lines. Observational confirmations of the Raman scattering mechanism include the spectropolarimetry which shows that the features are highly polarized in contrast with other negligibly polarized lines (*e.g.* Schmid & Schild 1994). The identification of the Raman scattering nature is corroborated by the UV observation by Espey et al. (1995), who showed that the symbiotic star RR Tel exhibits a very strong O VI doublet with the intense broad features around $\lambda 6827$ and $\lambda 7088$.

Valuable kinematic information on the emission nebula of a symbiotic system is obtained in a detailed analysis of the profiles of the emission lines, which often accompany non-trivial structures including double-peaked or partial absorption troughs (*e.g.* Mueller & Nussbaumer 1985, Pereira et al. 1995). The Raman scattered features can provide a useful diagnostic to constrain many kinematical parameters of a symbiotic system, because they have broadened profiles due to the relative motion of the stellar wind around the cool giant with respect to the emission nebula. Furthermore, the width of the profiles is also enhanced by the inelastic nature of the scattering by almost an order of magnitude.

Recently Harries & Howarth (1996, 1997) provided a good amount of spectropolarimetric data and performed a fairly complete Monte Carlo calculation about the Raman scattered emission features (see also Schmid 1996). In their observational data some symbiotic stars show the polarization direction flip around the red part of the Raman scattered feature. This kind of behavior usually accompanies multiple peak structures in the polarized flux (*e.g.* Espey et al. 1995, Schmid 1996). However, in the spherical wind model, many Monte Carlo computations show that the polarization flip usually occurs around the center of the feature calling a need to investigate non-spherical models.

This is the second paper in a series on the polarization and the line profiles of the Raman scattered flux. In Lee & Lee 1997 (hereafter Paper I), we reviewed the basic atomic physics of the Raman scattering of incident photons shortward of Ly α by hydrogen atoms, and computed the profiles and the polarization for a few cases using the single scattering approximation (see also Lee & Lee 1996). A more complete review about the atomic physics is provided by Isliker et al. (1989) and the references therein. In this paper we calculate the line profiles and the polarization of the Raman scattered O VI lines for various kinematic models using a Monte Carlo method.

The paper is composed as follows. In section 2, the basic procedures of the Monte Carlo method and the model descriptions are given. Using the Monte Carlo code we investigate some fundamental properties of the Rayleigh-Raman scattering processes and discuss them in section 3. The results of the numerical calculations are presented in section 4. In section 5, observational implications are commented. Finally, in section 6, a summary is presented with discussions about the significance of spectropolarimetry in understanding the symbiotic systems.

2. Model

There has been much observational work on symbiotic systems, showing that complicated kinematics is responsible for variabilities and complex structures in the line profiles (*e.g.* Mueller & Nussbaumer 1985, Pereira et al. 1995). We do not attempt to give a detailed dynamical model in this work, but adopt rather simple models in order to find out the main features contributing to the polarization structures and the profiles in the Raman scattered lines (*e.g.* Harries & Howarth 1996, Schmid 1996). In particular, the polarization behavior is expected to depend upon the scattering optical depth of the system, which naturally measures the number of scatterings before a given photon gets into the line of sight. The Raman scattering of the O VI photons is also characterized by an enhanced Doppler effect, according to which the wavelength shift of an incident photon increases by a factor of ~ 7 . Therefore, the kinematics of the scatterers may combine with the scattering optical depth structure to contribute to the complicated behavior of the polarization of the Raman scattered features.

In this section, we summarize the basic points of the Monte Carlo code and the kinematic models adopted in our numerical simulations. For the Raman and Rayleigh scattering cross sections of the O VI doublets, we use the results in Paper I, in which we showed that

$$\begin{aligned}\sigma_{Ram}(1032) &= 7.5 \sigma_T, \quad \sigma_{Ram}(1038) = 2.5 \sigma_T \\ \sigma_{Ray}(1032) &= 34 \sigma_T, \quad \sigma_{Ray}(1038) = 6.8 \sigma_T\end{aligned}\tag{2.1}$$

where $\sigma_T = 6.6 \times 10^{-25} \text{ cm}^2$ is the Thomson scattering cross section.

2.1 Monte Carlo Method

In this subsection we briefly describe the Monte Carlo method to compute the profiles and the polarization of the Raman scattered O VI doublet lines. It is first assumed that there is an emission region embedded in the scattering medium consisting of the extended atmosphere of the cool giant. The incident UV line photons are further assumed to be emitted isotropically and unpolarized. We start with the incident photons governed by a Gaussian profile corresponding to a Maxwell-Boltzmann distribution. We subsequently investigate the cases where the incident radiation field is described by synthetic profiles such as double-peaked profiles often seen in the observational data.

In Fig. 1 we show a schematic geometry of a symbiotic star system, which is adopted for our Monte Carlo calculation. The coordinate system is chosen in such a way that the binary axis coincides with the z -axis and the observer's line of sight is the x -axis. The hot star is represented by the circle on the right side, and the bigger circle in the origin is the

cool giant. A spherically symmetric stellar wind is depicted by radial arrows around the cool giant.

For a numerical simulation of the Rayleigh-Raman scattering it is essential to compute the free path length at a position for a given wave vector and wavelength. The mean free path of a UV line photon is given

$$l_f = (n\sigma_{tot})^{-1}, \quad (2.2)$$

where the total scattering cross section σ_{tot} is defined by

$$\sigma_{tot} \equiv \sigma_{Ram} + \sigma_{Ray}. \quad (2.3)$$

A given photon travels up to a distance l with a probability

$$p_l = 1 - \exp(-l/l_f) = 1 - \exp(-\tau_l), \quad (2.4)$$

where

$$\tau_l \equiv l/l_f = \int ds n(s)\sigma_{tot}. \quad (2.5)$$

In terms of a random uniform variable r in an interval between 0 and 1, τ_l can be generated by a transformation

$$\tau_l = -\ln(1 - r), \quad (2.6)$$

identifying r with p_l . The inverse transformation of Eq. (2.5) gives the free path length of the incident photon.

A photon travels a free path l before a hydrogen atom Raman-scatters it with a branching ratio $r_{Ram} \equiv \sigma_{Ram}/\sigma_{tot}$. If a random number is greater than r_{Ram} , then we regard this scattering as Rayleigh, and otherwise the photon is Raman-scattered.

When the scattering type is Rayleigh, the escape condition should be examined before the next scattering site is determined. The escape condition is simply

$$\tau_l \geq \tau_{esc}, \quad (2.7)$$

where τ_{esc} is the scattering optical depth to an observer at infinity, *i.e.*,

$$\tau_{esc} = \int_s^\infty ds n(s)\sigma_{tot}. \quad (2.8)$$

If the escape condition is met, then the UV photon is regarded as being emitted to infinity. Otherwise a new wave vector and the polarization components are calculated to be used for the subsequent scattering.

On the other hand, if the photon is Raman-scattered, then we record the photon with the polarization according to the wavelength. Here, we assume that the continuum absorption around H α is negligible and that the Raman-scattered photon escapes freely. The effect of continuum opacity has been extensively investigated by Schmid (1992, 1996) and Harries & Howarth (1997). In order to keep the standard deviation no larger than 1.5 percent, we generate typically 5×10^6 photons for each run.

In the following section, we discuss the stellar wind models and calculate the relevant scattering optical depths and the escape conditions.

2.2 Stellar Wind Models

We discussed the kinematic models in Paper I, which we adopt and again introduce in this paper (see also Nussbaumer & Vogel 1987). A typical wind velocity law can be written as

$$\begin{aligned}\mathbf{v}(\mathbf{r}) &= v_\infty (1 - R_*/r)^\beta \hat{\mathbf{r}} \\ &= v_\infty (1 - \rho^{-1})^\beta \hat{\mathbf{r}},\end{aligned}\tag{2.9}$$

where v_∞ is the terminal wind velocity, R_* is the radius of the cool giant, $\rho \equiv r/R_*$ is the radial distance in the unit of R_* , and β is a positive constant. The density profile corresponding to the velocity law Eq. (2.9) is given by

$$n(\mathbf{r}) = n_0 \rho^{-2} (1 - \rho^{-1})^{-\beta},\tag{2.10}$$

where n_0 is a typical density given in terms of the mass loss rate \dot{M} , and the proton mass m_p by

$$n_0 \equiv \dot{M}/4\pi R_*^2 m_p v_\infty.\tag{2.11}$$

We again choose $\beta = 1$ as in Paper I.

Therefore, the total scattering optical depth between position 1 and position 2 is given by

$$\begin{aligned}\tau_{12} &= \int_{s_1}^{s_2} ds n(\mathbf{r}) \sigma_{tot} \\ &= \tau_0 \int_{\rho_1}^{\rho_2} \frac{d\rho}{\sqrt{\rho^2 - b^2}} \frac{1}{(\rho - 1)},\end{aligned}\tag{2.12}$$

where s is the running parameter along the photon path, and the representative scattering optical depth

$$\tau_0 \equiv n_0 R_* \sigma_{tot}.\tag{2.13}$$

Here, b is the impact parameter of the photon path with respect to the center of the cool giant divided by R_* (see Fig. 1 for a schematic geometry). In this paper, it is understood that all the distances are measured in units of the radius of the cool giant R_* .

If the i -th scattering site is given by $\vec{\rho}_i$ and the wave vector by $\hat{\mathbf{k}}_i$, the next scattering site $\vec{\rho}_{i+1}$ characterized by the scattering optical depth τ_i from $\vec{\rho}_i$ is obviously given by

$$\begin{aligned}\vec{\rho}_{i+1} &= \vec{\rho}_i + |\vec{\rho}_{i+1} - \vec{\rho}_i| \hat{\mathbf{k}}_i \\ &= \vec{\rho}_i + s_i(\tau_i) \hat{\mathbf{k}}_i,\end{aligned}\tag{2.14}$$

where $s_i(\tau_i)$ is the distance between the two scattering sites, which is dependent on the vectors $\vec{\rho}_i$, $\hat{\mathbf{k}}_i$ and τ_i .

The functional form of s_i can be written separately for the case where the impact parameter of the photon trajectory is larger than the radius of the cool giant and for the case where it is smaller than the radius of the giant, *i.e.*, either $b > 1$ or $b < 1$.

In order to express the functional form of $s_i(\tau_i)$, we perform an integration of Eq. (2.12). Introducing a function $f(\rho)$ defined by

$$f(\rho) \equiv \frac{1}{\sqrt{|1-b^2|}} \left[\rho + \sqrt{\rho^2 - b^2} - 1 \right] \quad (2.15)$$

we have an equivalent relation

$$\rho = \frac{1}{2} \left[1 + \sqrt{|1-b^2|} f(\rho) + b^2 \{ (1 + \sqrt{|1-b^2|} f(\rho)) \}^{-1} \right], \quad (2.16)$$

which gives ρ after $f(\rho)$ is obtained.

If $b < 1$, then we obtain

$$\begin{cases} f(\rho_{i+1}) = \coth \left[\coth^{-1} f(\rho_i) - \frac{\sqrt{1-b^2}}{2} \frac{\tau_i}{\tau_0} \right] \\ s_i(\tau_i) = \sqrt{\rho_{i+1}^2 - b^2} - \sqrt{\rho_i^2 - b^2} \end{cases} \quad (2.17)$$

for $\hat{\mathbf{k}}_i \cdot \hat{\mathbf{r}} > 0$, and

$$\begin{cases} f(\rho_{i+1}) = \coth \left[\coth^{-1} f(\rho_i) + \frac{\sqrt{1-b^2}}{2} \frac{\tau_i}{\tau_0} \right] \\ s_i(\tau_i) = \sqrt{\rho_i^2 - b^2} - \sqrt{\rho_{i+1}^2 - b^2} \end{cases} \quad (2.18)$$

for $\hat{\mathbf{k}}_i \cdot \hat{\mathbf{r}} < 0$.

On the other hand, if $b > 1$, then the result is

$$\begin{cases} f(\rho_{i+1}) = \tan \left[\tan^{-1} f(\rho_i) + \frac{\sqrt{b^2-1}}{2} \frac{\tau_i}{\tau_0} \right] \\ s_i(\tau_i) = \sqrt{\rho_{i+1}^2 - b^2} - \sqrt{\rho_i^2 - b^2} \end{cases} \quad (2.19)$$

for $\hat{\mathbf{k}}_i \cdot \hat{\mathbf{r}} > 0$. If $b > 1$ and $\hat{\mathbf{k}}_i \cdot \hat{\mathbf{r}} < 0$, then we introduce the scattering optical depth τ_b to the impact point, which is given by

$$\tau_b = \frac{2\tau_0}{\sqrt{b^2-1}} \left[\tan^{-1} f(\rho_i) - \tan^{-1} f(b) \right]. \quad (2.20)$$

Then the final result is written as

$$\begin{cases} f(\rho_{i+1}) = \tan \left[\tan^{-1} f(\rho_i) - \frac{\sqrt{b^2-1}}{2} \frac{\tau_i}{\tau_0} \right] \\ s_i(\tau_i) = \sqrt{\rho_i^2 - b^2} - \sqrt{\rho_{i+1}^2 - b^2} \end{cases} \quad (2.21)$$

for $\tau_i < \tau_b$, and

$$\begin{cases} f(\rho_{i+1}) = \tan \left[\tan^{-1} f(b) + \frac{\sqrt{b^2 - 1}}{2} \frac{\tau_i}{\tau_0} \right] \\ s_i(\tau_i) = \sqrt{\rho_i^2 - b^2} + \sqrt{\rho_{i+1}^2 - b^2} \end{cases} \quad (2.22)$$

for $\tau_i > \tau_b$.

The escape conditions are met when the scattering optical depth $\tau_i \geq \tau_{esc}$. Here, the escape scattering optical depth τ_{esc} is obtained from Eqs. (2.17)-(2.22) by letting $s_i \rightarrow \infty$, *i.e.*,

$$\tau_{esc} = \begin{cases} \frac{2\tau_0}{\sqrt{1-b^2}} \coth^{-1} f(\rho_i), & \text{for } b < 1, \hat{\mathbf{k}}_i \cdot \hat{\mathbf{r}} > 0; \\ \frac{2\tau_0}{\sqrt{b^2-1}} \left[\frac{\pi}{2} - \tan^{-1} f(\rho_i) \right], & \text{for } b > 1, \hat{\mathbf{k}}_i \cdot \hat{\mathbf{r}} > 0; \\ \frac{2\tau_0}{\sqrt{b^2-1}} \left[\frac{\pi}{2} - \tan^{-1} f(b) \right], & \text{for } b > 1, \hat{\mathbf{k}}_i \cdot \hat{\mathbf{r}} < 0. \end{cases} \quad (2.23)$$

No escape is possible for the case where $b < 1$ and $\hat{\mathbf{k}}_i \cdot \hat{\mathbf{r}} < 0$, because the total optical depth to the surface of the cool giant diverges for all ρ_i . This means that the photons are scattered off before they reach the surface of the cool giant.

The final procedure of the Monte Carlo simulation is to determine the Doppler factors and the polarization associated with the scattered photon. The polarization state of an ensemble of photons is described by a density matrix (*e.g.* Berestetskii et al. 1971, Lee et al. 1994), where the Stokes parameters Q , U , and V correspond to the difference of the main diagonal elements, the real and the imaginary parts of the off-diagonal elements of the density matrix, respectively. The Rayleigh-Raman scattering is characterized by the Rayleigh phase function, and the wave vector and the polarization of the scattered photon are computed by the same way as in the case of the Thomson scattering.

For the Raman scattering of the O VI doublets, the total wavelength shift is given by

$$\frac{\Delta\lambda_f}{\lambda_f} = \frac{\lambda_f}{\lambda_i} \frac{\hat{\mathbf{k}}_i \cdot \mathbf{v}(\mathbf{r})}{c} + \frac{\hat{\mathbf{k}}_f \cdot \mathbf{v}(\mathbf{r})}{c} \quad (2.24)$$

where $\hat{\mathbf{k}}_i$ is the wave vector of the incident photon and $\hat{\mathbf{k}}_f$ is that of the outgoing photon. Eq. (2.24) is also valid for Rayleigh scattering, where $\lambda_f = \lambda_i$. It is clear that in the case of Raman scattering the Doppler factor becomes large by a factor of about 7 due to the motion of the scatterers relative to the emission source. We show the contours of constant total scattering optical depth and Doppler factors in Fig. 2, which were introduced and discussed in Paper I.

3. Fundamental Properties of Raman Scattering

In this section we discuss the characteristic features of the Raman scattering process using the Monte Carlo method. Schmid (1992, 1995, 1996) also discussed the basic properties of the Rayleigh-Raman scattering process (see also Harries & Howarth 1997) and we

elaborate further the properties of the scattering process in a similar way to deal with the random walk process.

3.1 Single Scattering Approximation

In Paper I, we briefly mentioned the single scattering approximation, which applies to the case where the scattering region is characterized by a small scattering optical thickness. This formalism can also be useful as a check of our Monte Carlo code, in the sense that it is the limiting case when the total scattering optical depth tends to zero.

In Fig. 3 we present a result from our Monte Carlo code for a scattering optical depth $\tau_0 = 0.5$ and compare it with the corresponding result from the single scattering approximation. The adopted parameters are described in Paper I. The Monte Carlo result is in good agreement with the result from the single scattering approximation within one standard deviation shown by the error bars in the degree of polarization.

In the following subsection we quantify the single scattering approximation and investigate some fundamental properties of the Rayleigh-Raman scattering process.

3.2 Reflection from a Slab

A UV photon with a wavelength shorter than 1216 \AA can be scattered either by a Rayleigh process or by a Raman process from a hydrogen atom. Therefore, the UV photon may be Rayleigh-scattered several times before it is Raman-scattered. Under the assumption that a Raman-scattered photon has a very small optical depth, it will escape freely from the scattering region and may reach the observer. The ratio of the number of the emergent photons which are Raman-scattered to that of the total incident photons is expected to be dependent on the ratio of the Raman scattering cross section to the total scattering cross section and the scattering geometry such as the total optical depth of the medium.

In this subsection, we discuss briefly some of the fundamental properties of the Rayleigh-Raman scattering process of UV line photons in a simple scattering medium.

H. Schmid, who proposed the Raman process in symbiotic systems and performed pioneering works in this subject, presented the basic results in his papers (*e.g.* Schmid 1992, Schmid 1996). A Monte Carlo simulation is particularly useful in describing the scattering process, because we can conceptually divide the emergent photons according to their scattering numbers and perform a detailed analysis. Pursuing in this line of reasoning, we collect the photons reflected from the both sides of a slab of finite scattering optical depth, using the Monte Carlo code. It is assumed that the slab is illuminated from outside and that the distance from the slab to the incident radiation source is much larger than the size of the slab, so that the incident photons enter the slab effectively normally. The emergent photons are subsequently divided into their number of scatterings, and we record their flux and the degree of polarization for further analysis.

Fig. 4 illustrates the result from the Monte Carlo calculation on the Rayleigh and Raman reflected components from a finite slab as a function of the number of scatterings. On the vertical axis is shown the logarithm of the number of the photons reflected from the slab. The total scattering optical depth τ_s of the slab is chosen to be $\tau_s = 0.5, 1, 5, 10$. The ratio $r_{Ray} \equiv \sigma_{Ray}/\sigma_{tot}$ of the Rayleigh scattering cross section to the total scattering

cross section is taken to be $r_{Ray} = 0.2, 0.8$, where the case $r_{Ray} = 0.2$ is represented by the light lines and the thick lines are for the $r_{Ray} = 0.8$ case.

When the scattering optical depth is small and $r_{Ray} = 0.8$, the Rayleigh-scattered flux is larger than the Raman-scattered flux, whereas the converse is true for large scattering optical depths. This is because the Rayleigh-scattered photons are trapped as the scattering optical depth increases, whereas all the Raman-scattered photons are assumed to escape on the spot.

As is usually expected the main contribution to the scattered flux is due to singly scattered photons. Both the flux and the degree of polarization show exponential decrease as a function of the number of scatterings. This behavior is the foundation of the single scattering approximation discussed in the previous section and in Paper I.

We may give a semi-quantitative argument about the fraction of the Raman scattered flux to the total incident flux. For a given slab of total scattering optical depth τ_s , a fraction $(1 - e^{-\tau_s})$ will be scattered at least once. Let's denote the total incident number flux by f_0 . Then $f_s \equiv f_0(1 - e^{-\tau_s})$ is the total scattered (number) flux. Let $f(n)$ be the number flux scattered no less than n . From this definition, it is obvious that

$$f(1) = f_s. \quad (3.1)$$

Furthermore, a fraction $(1 - r_{Ray})$ of f_s will be Raman scattered and escape the region. Hence if we denote by $f_{Ram}(n)$ the Raman scattered (number) flux scattered only n times, then

$$f_{Ram}(1) = (1 - r_{Ray})f_s = (1 - r_{Ray})f(1). \quad (3.2)$$

In fact, this relation holds for any n , that is,

$$f_{Ram}(n) = (1 - r_{Ray})f(n), \quad (3.3)$$

because any Raman scattered photon does not suffer a subsequent scattering.

In a similar way we denote by $f_{Ray}(n)$ the Rayleigh scattered emergent number flux scattered only n times. Then we may write

$$f_{Ray}(n) = r_{Ray}\beta(n)f(n). \quad (3.4)$$

Here, the function $\beta(n)$ is loosely defined as an escape probability from the n -th scattering site. Because the scattering process is similar to the random walk process, there is no definite site of n -th scattering, and we can only state in a probabilistic way. If we borrow from the solution of the random walk problem, we may state that the photon diffuses up to the position where the scattering optical depth from the surface is approximately \sqrt{n} . Therefore, we may tentatively set

$$\beta(n) = \frac{1}{2}(e^{-\sqrt{n}} + e^{-(\tau_s - \sqrt{n})}). \quad (3.5)$$

When the number of scattering exceeds τ_s^2 , then the above formula does not give any meaningful results. However, the flux $f(n)$ decreases approximately exponentially, the result will not be sensitive to the choice of $\beta(n)$ for sufficiently large n .

Having defined $f_{Ram}(n)$, $f_{Ray}(n)$, and $\beta(n)$, we can formally give a recursion formula for $f(n)$, which is

$$\begin{aligned} f(n+1) &= f(n) - f_{Ram}(n) - f_{Ray}(n) \\ &= r_{Ray}[1 - \beta(n)]f(n). \end{aligned} \quad (3.6)$$

The functional dependence of $\beta(n)$ on the scattering optical depth and the scattering geometry determines the basic properties of the Rayleigh-Raman scattering process.

In Fig. 5 we plot $f_{Ram}(n)$, $f_{Ray}(n)$ as a function of the scattering number n , which are obtained recursively using Eq. (3.6). A comparison is made with the corresponding Monte Carlo results. The solid lines show the Monte Carlo results and the dotted lines give $f_{Ram}(n)$ and $f_{Ray}(n)$ obtained analytically. Eq. (3.5) is used for the escape probability for the upper panel. In the bottom panel we show a different set of $f_{Ram}(n)$ and $f_{Ray}(n)$ using another formula for the escape probability, defined by

$$\beta'(n) = \frac{1}{2} \exp(-n^{0.4}). \quad (3.7)$$

The adopted parameters are $\tau_s = 10$, and $r_{Ray} = 0.8$, which is relevant for the O VI doublets $\lambda\lambda 1032, 1038$. Due to the choice of the parameters we see that the Raman-scattered fluxes are larger than the Rayleigh-scattered counterpart. As is shown in Fig. 5a, the agreement is very good except when the number of scatterings becomes large, where the small remainder flux does not give much significance. Far better agreement is obtained in Fig. 5b. Considering the agreement shown in Fig. 5, the preceding argument may be said to closely describe the scattering process in the scattering medium.

The total Raman scattered flux F_{Ram} is given by

$$F_{Ram} = \sum_n f_{Ram}(n) = (1 - r_{Ray}) \sum_n f(n). \quad (3.8)$$

Similarly, we may write the total Rayleigh scattered flux F_{Ray}

$$F_{Ray} = \sum_n f_{Ray}(n) = r_{Ray} \sum_n \beta(n) f(n). \quad (3.9)$$

Hence, we can estimate the ratio R_{Ram} of the total Raman scattered flux to that of the Rayleigh scattered flux

$$\begin{aligned} R_{Ram} &\equiv F_{Ram} / F_{Ray} \\ &= \frac{(1 - r_{Ray})}{r_{Ray}} R_s, \end{aligned} \quad (3.10)$$

where

$$R_s = \frac{\sum_n f(n)}{\sum_n \beta(n) f(n)}. \quad (3.11)$$

For sufficiently large τ_s , $\beta(n)$ decreases for small n . Because $f(n)$ is decreasing sufficiently fast, the ratio R_s is dominantly affected by the sum of the first few terms. A conservative estimate can be obtained by considering only the first term, which gives

$$R_{Ram}^{(1)} = \frac{(1 - r_{Ray})}{\beta(1) r_{Ray}}. \quad (3.12)$$

Here, in the limiting case where $\tau_s \rightarrow \infty$, $\beta(1)$ can be evaluated exactly from the first principle, which is simply

$$\begin{aligned}\beta^{exact}(1) &= \int_0^\infty dt e^{-t} \int_0^1 d\mu \frac{3}{8}(1 + \mu^2)e^{-t/\mu} \\ &= (11 - 12 \ln 2)/16 \sim 0.168.\end{aligned}\tag{3.13}$$

This is approximately equal to $(2e)^{-1}$ given either by Eq. (3.5) or by Eq. (3.7). Hence for $r_{Ray} = 0.8$, which is close to the true value of the O VI doublets, we have $R_{Ram}^{(1)} = 1.48$ using β^{exact} . This ratio is a typical one when the scattering optical depth is moderately larger than 1.

For a slab of $\tau_s = 10$, if we include terms up to $n = 20$, the ratio becomes $R_{Ram} = 2.11$ which differs with $R_{Ram}^{(1)}$ significantly. Note that this number is sensitively dependent on the total scattering optical depth τ_s of the slab and that it usually increases with τ_s . This implies that even though the Rayleigh scattering cross section is much larger than that of the Raman scattering cross section, the emergent Raman scattered flux is comparable to or larger than that of the emergent Rayleigh scattered flux, when the medium is not optically thin. This is also confirmed by Schmid (1992) and by Harries & Howarth (1997).

For a small scattering optical thickness, the flux ratio of the reflected components is fairly close to the ratio of the scattering cross sections because the effect of multiple scattering is negligible. In the above formalism, this can be shown in a straightforward way. That is, $f(n) \sim 0$ for $n \geq 2$, and we may take $\beta(1) \sim 1$. Therefore, we have

$$R_{Ram} \sim R_{Ram}^{(1)} = \frac{1 - r_{Ray}}{r_{Ray}} = \frac{\sigma_{Ram}}{\sigma_{Ray}},\tag{3.14}$$

which implies that no conversion to Raman scattering from Rayleigh scattering occurs significantly.

4. Numerical Results

In this section, we discuss the results of our Monte Carlo calculation for various cases including non-spherical wind models. The largest polarization is expected for 90 degree scattering, and negligible polarization is obtained for forward and backward scatterings. In this section the photons collected from the numerical simulations are those escaping perpendicular to the binary axis unless stated otherwise. Because of the symmetry about the binary axis in spherical wind models the polarization direction is either along the binary axis or perpendicular to it. Therefore we denote by negative P the polarization along the binary axis and by positive P the polarization perpendicular to it.

4.1 Simple Gaussian Case

The physical conditions of the emission line region are not known in detail, and we assume that it is in thermal equilibrium with a temperature T_{em} , being located very near

to the hot star. Under this assumption, the profile of the emission line is described by a Gaussian with the width of

$$v_{th} = \sqrt{2kT_{em}/m_a} = 2.3 T_{em,4}^{1/2} \text{ km s}^{-1}, \quad (4.1)$$

where $T_{em,4} \equiv T_{em}/(10^4 \text{ K})$, and the oxygen atomic mass $m_a = 16 m_p$, m_p being the proton mass. We take the wind terminal velocity $v_\infty = 20 \text{ km s}^{-1}$, $R_* = 50R_\odot$ and the separation of the cool giant and the hot star $a = 10R_*$ as in Paper I. From now on, we will refer this case as the simple Gaussian case, which will serve as a reference model throughout the paper.

In Fig. 6 we show the line profiles and the polarization for both $\lambda 1032$ and $\lambda 1038$ photons for the cases where $\tau_0 = 0.5, 1.0, 10$.

The polarization behavior and the line profiles are similar to those of the single scattering case, where the large polarization perpendicular to the binary axis is shown with small flux in the blue part of the feature and the polarization becomes small in the center and red parts of the feature. Furthermore, the polarization direction changes around the center part of the feature when $\tau_0 \gtrsim 5$. When $\tau_0 \lesssim 1$, the total flux shows a double-peaked profile and in the case of opposite limit, a broad single-peaked profile is obtained. This is already summarized in Paper I and also by Harries & Howarth (1997) (see also Schmid 1996).

It is noted that the single scattering approximation gives a good qualitative description when $\tau_0 \lesssim 10$. Another important point to note is that the scattering region corresponding to the polarization flip is the region which is characterized by the Doppler factor about zero, that is, the sphere having the binary axis connecting the hot component and the cool giant as a diameter. We may give a simple intuitive explanation for this phenomenon in the context of the single scattering approximation as follows.

The boundary region for the polarization direction flip is the conical region with the opening angle of $\pi/4$ with the apex at the hot component. From Fig. 2, the scattering region responsible for the blue shift is mostly inside the conical region giving strong polarization perpendicular to the binary axis. However, in the center-red part there is a competition of the two polarization components because the region with Doppler factors 0 and larger lies both inside and outside the conical region. The contribution outside the conical region increases as the typical scattering optical depth τ_0 becomes large. This explains the phenomenon that the polarization flip around the central region is obtained clearly when τ_0 is significantly larger than 1.

4.2 Extended Ionized Region

The assumption that the UV emission line region is spatially point-like is rather naive and the scattering region reduces severely due to the extended emission line region. Several researchers investigated the detailed shape of the emission nebula around the hot component of a symbiotic system. Seaquist et al. (1984) provided the shape of the ionization front using a parameter X_H defined by

$$X_H \equiv \frac{4\pi a L_H}{\alpha_B} \left(\frac{m_p v^2}{M} \right) \quad (4.2)$$

where L_H is the total luminosity of the ionizing radiation, \dot{M} is the mass loss rate of the cool giant, v is the wind speed, a is the separation of the cool giant and the hot component, and α_B is the case B recombination coefficient for hydrogen. Monte Carlo calculations for various values of X_H have been done for the Rayleigh scattering of UV radiation (Schmid 1995) and also for the Raman scattering of the O VI lines (Schmid 1996, Harries & Howarth 1997). We show some of our results to point out the profile and polarization features affected by the parameter X_H .

We consider three cases where the parameter X_H is given by $X_H = 0.04, 0.4, 4.0$. For a value of $L_H = 130L_\odot$, where L_\odot is the solar luminosity, the corresponding mass loss rates of the cool giant are $\dot{M} = 10^{-7}, 10^{-6}, 10^{-5} M_\odot \text{ yr}^{-1}$. In Fig. 7 is shown a typical ionization structure around the hot star. The solid lines represent the ionization front for the H II region, and the dashed lines are the conic sections which we adopt to approximate the true location of the front (*i.e.* the solid lines) in order to speed up the numerical calculation.

The O VI line photons originate deep inside the H II region, because O VI has much higher ionization potential than H I does. Therefore, we assume that the O VI region is well-localized around the hot star, having a small size compared with that of a typical scattering geometry and justifying the point-source assumption. The results are presented in Fig. 8, where we only show the cases $\tau_0 = 1, 10$ for the $\lambda 1032$ photons.

The overall results are qualitatively similar to those of the simple Gaussian case described in the preceding section. However, when X_H gets as large as ~ 4 , the polarization is dominated by the component perpendicular to the binary axis, and no polarization flip is seen around the center of the feature. A simple explanation of this behavior is that the extended H II region has more intersection with the scattering region responsible for the parallel component of the polarization than the region giving the perpendicular component in the simple Gaussian case (*cf.* section 4.1). Therefore, compared with the simple Gaussian case, the reduced scattering region for the parallel component results in the perpendicular polarization on the whole. This tendency is intensified as X_H increases. Hence combined with the analysis of section 4.1 the polarization perpendicular to the binary axis is stronger as X_H increases and τ_0 decreases, which is displayed by the lower left panel of Fig. 7.

4.3 Disk Wind

As a non-spherical model a disk wind is invoked and described in this subsection. For ease of Monte Carlo coding, we just exclude the conic section of the spherical stellar wind from the scattering region. That is, the stellar wind is described by

$$\mathbf{v}_{disk}(\rho, \theta_y) = \begin{cases} v_\infty(1 - \rho^{-1})^\beta \hat{\mathbf{r}} & \text{if } \theta_o \leq \theta_y \leq \pi - \theta_o \\ 0 & \text{if otherwise} \end{cases} \quad (4.3)$$

where θ_o is the opening angle of the disk wind. Here, the normal direction of the disk is chosen to be the y -axis and the z -axis coincides with the binary axis. The angle θ_y is defined as the angle making with the y -axis, *i.e.* ,

$$\theta_y \equiv \tan^{-1} \frac{\sqrt{x^2 + z^2}}{y} \quad (4.4)$$

The density law is given in a similar way as in Eq. (4.3).

In Fig. 9 we display the numerical results from the disk wind with an opening angle $\theta_0 = \pi/4$. The results are displayed separately for the two cases. In the first case the observer sees the symbiotic system from the equatorial plane (Fig. 9a) and in the other case the observer is on the polar direction (Fig. 9b). Even though the azimuthal symmetry about the binary axis is broken, the dominant polarization turns out to be either along the binary axis or perpendicular to it, and hence we keep the convention of the polarization sign to denote the direction of polarization.

In both the cases the profiles and the degree of polarization are qualitatively similar to those of the simple Gaussian case. The plausible explanation for the results is that in the range where the single scattering approximation is a valid one the same Doppler- τ_s contour diagram (Fig. 2) applies and therefore a similar argument leads to the qualitatively same results.

4.4 Bipolar Flow

As another application of non-spherical wind models, we investigate a bipolar wind, which is simplified as a truncated spherical wind model in a similar way to the disk wind case described in the previous subsection. The wind symmetry axis is assumed to be perpendicular to the binary axis. Therefore, the velocity law is

$$\mathbf{v}_{bipol}(\rho, \theta_y) = \begin{cases} 0 & \text{if } \theta_o \leq \theta_y \leq \pi - \theta_o \\ v_\infty(1 - \rho^{-1})^\beta \hat{\mathbf{r}} & \text{if otherwise} \end{cases} \quad (4.5)$$

The numerical results are displayed in Fig. 10, where the wind opening angle $\theta_o = \pi/4$. In the left panel, the observer's line of sight is perpendicular both to the bipolar wind direction and to the binary axis, whereas in the right panel the observer lies in the direction of the wind.

Unlike the disk wind case, we do not see any polarization flip in the bipolar wind model. This is again explained in a similar way to the case of the extended ionized region, where a large fraction of the scattering region responsible for polarization flip in Fig. 2 is excluded in the bipolar wind model. Therefore, the overall behavior of the polarization is characterized by a large degree of polarization in the blue part of the feature and the existence of residual polarization and flux in the red most part.

4.5 Synthetic Profiles

Some of symbiotic systems exhibit complex features in their emission lines. The detailed physical nature of the emission line region of a symbiotic system is controversial and the velocity scale associated with the stellar wind around the hot star is sometimes of order 10^3 km s^{-1} (e.g. Vogel & Nussbaumer 1994). Osterbrock(1970) proposed that synthetic line profiles composed of triangular shape may approximate the observed profiles quite well in the planetary nebula IC 418. We also use single-peaked and double-peaked triangular synthetic profiles to compute the profiles and polarization of the Raman scattered lines.

The parameters necessary to describe the profiles are the widths and the peak values. In this work, the half width at the bottom of the single-peaked triangular profile is assumed

to be 30 km s^{-1} . For the double-peaked triangular profile we superpose the two single-peaked triangular profiles with different peak values. The ratio of the peak values in the double-peaked profile is taken to be 0.3.

In the right panel of Fig. 11 are displayed the Monte Carlo results for a single-peaked profile. The input profiles are shown in a small box at upper right corner in each panel of Fig. 11. As stated in Paper I synthetic profiles can be decomposed into δ -function profiles, which is the basis of the Green function formalism. In this regard, we see a large degree of polarization of the blue part of the feature, reminiscent of the simple Gaussian case discussed in section 4.1.

In the left panel of Fig. 11 we show the corresponding results for a double-peaked profile. There are two peaks in the degree of polarization corresponding to the blue wing of each triangular peak. Therefore, the locations of the peaks in the degree of polarization shift to the blue with respect to those of the scattered fluxes. The amount of the shift depends mainly on the wind terminal velocity, and it increases as the wind velocity gets larger. Hence, the wind terminal velocity can be constrained by the shift of the peaks in the polarized flux with respect to the total scattered flux.

5. Effect of Binary Motion

It is expected that the hot component and the cool giant of a symbiotic star revolve around their center of mass with a velocity

$$v_{rev} = \sqrt{G\mu/a} = 30 \left(\frac{\mu_1}{a_1} \right)^{1/2} \text{ km s}^{-1}, \quad (4.6)$$

where $\mu_1 = \mu/(1 M_\odot)$ is the reduced mass of the hot component and the cool giant in terms of the solar mass and $a_1 = a/(1 \text{ AU})$ is the separation of the two components in the astronomical unit. This velocity scale is comparable to the terminal wind velocity and therefore may affect significantly on the profiles and the polarization of the Raman scattered features. However, it is known phenomenologically that the typical separation a of the ‘S’ type symbiotic stars is very different from that of the ‘D’ type symbiotics (*e.g.* Iben & Tutukov 1996). In this respect, the spectropolarimetry monitored for an extended term will reveal a good deal of information about kinematics. In this section, we investigate the effect of the orbital motion of the hot component with respect to the cool giant on the profiles and the polarization of the Raman scattered features.

In Fig. 12 we draw the Doppler factor- τ_s contours analogous to Fig. 2, where the hot component is moving in $-y$ direction with velocity $v_{rev} = 0.6 v_\infty$, and the observer’s line of sight coincides with x -direction. The τ_s contour remains the same because it is assumed that the wind structure around the cool giant remains spherically symmetric in the rest frame of the cool giant and the scattering cross section is insensitive to the velocity scale of order $v_\infty = 20 \text{ km s}^{-1}$. The diagram is plotted in the rest frame of the cool giant. Due to the enhancement of the Doppler factor, the relative motion of the cool giant with respect to the observer is not important compared with the motion of the photon source relative to the scatterers.

Notable changes are seen in the structure of the Doppler factors. The contour corresponding to zero Doppler factor is not spherical any more and the sphere connecting the two stars may be decomposed into the upper hemisphere with positive Doppler factors and the lower hemisphere with negative Doppler factors. The important point to note about this sphere is that in the case of simple Gaussian case (see section 4.1) the polarization flip occurs around this sphere, which corresponds to the central part of the scattered feature. Therefore, we can expect from this diagram that there is possibility of polarization flip in the red part and/or the blue part of the scattered feature.

The numerical results corresponding to the situation depicted in Fig. 12 are presented in Fig. 13, where the observer's line of sight is perpendicular to the orbital plane. Here, we also present the position angle because the symmetry about the binary axis is broken with the introduction of the relative motion of the hot component with respect to the cool giant. The position angle is not defined when the degree of polarization is 0. Therefore in the extreme red part where there is so small an amount of flux not to be assigned measurable polarization, the position angle is highly uncertain and does not yield any quantitative information.

When the scattering optical depth $\tau_0 = 1$ and $v_{rev} = 0.6 v_\infty$, the polarization flip occurs around the red part. The degree of polarization is strong in the blue part of the feature. The position angle remains almost perpendicular to the binary axis in this part and parallel in the red part of the feature. The polarization component perpendicular to the binary axis forms a double-peaked structure and therefore with the parallel component the overall polarization shows a triple-peaked structure. The triple-peaked structure is also seen in the polarized flux.

In the total scattered flux no obvious multiple structures are seen in these cases. The spectropolarimetry provided by Harries & Howarth (1996) shows that many symbiotic stars also have the multiple peak structures in the flux as well as in the polarization and the polarized flux. In the simple Gaussian case with small optical depth ($\tau_0 \leq 0.5$) there is a faint double peak structure in the flux. However, the small parameter space is not enough to explain the much more complicated phenomena shown by the observation. This strongly implies that the simple Gaussian profile of the incident radiation is difficult to explain the complicated behavior of the spectropolarimetry.

It is also noted that the polarization flip occurs at a scattering optical depth $\tau_0 = 1$. This is in contrast with the simple Gaussian case, where the polarization flip at the center part of the feature is obvious only when $\tau_0 \gtrsim 5$. This is particularly interesting considering the spectropolarimetry data on the symbiotic systems including RR Tel, where the polarization flip is clearly seen in the red part of the Raman-scattered features (*e.g.* Espey et al. 1995, Schmid & Schild 1990, Schild & Schmid 1996, Harries & Howarth 1996).

When the orbital velocity exceeds the wind terminal velocity, then the polarization flip is also shown in the blue part, which is illustrated in Fig. 14. Here, we adopt $v_{rev} = 3 v_\infty$. The polarization flip is seen in the red part and also in the blue part with small flux. This behavior may be explained using a similar argument mentioned in the preceding paragraphs with Fig. 11.

In Fig. 15, we show the numerical results when the observer's line of sight lies on the orbital plane. The results are similar to those of the simple Gaussian case, and therefore no polarization flip around the red part occurs in this case. This dramatically different

behavior can be also explained using the Doppler factor- τ_s diagram. When the observer's line of sight lies on the orbital plane, the section of the Doppler factor- τ_s diagram including the binary axis and perpendicular to the observer's line of sight coincides with Fig. 2, and the polarization behavior is not significantly different from that of the simple Gaussian case.

6. Observational Implications

Observational and evolutionary properties of symbiotic stars are extensively summarized by Iben & Tutukov (1996), according to whom symbiotic stars are rather inhomogeneous group showing a large range of variabilities and physical conditions. Detailed analysis of the UV emission lines of symbiotic stars also implies that kinematics around the emission line region may not be described by a simple unique model.

In the optically thin limit, the ratio of the $\lambda 1032$ flux to that of the $\lambda 1038$ flux in the O VI doublet is 2, which is the ratio of the oscillator strengths of the two transitions. However, this ratio is altered when the medium gets optically thick, where the stronger lines have more difficulty escaping the region. Far UV observations show that for the doublets including C IV $\lambda\lambda$ 1548, 1551, N V $\lambda\lambda$ 1238, 1241 the ratios are usually less than 2, and sometimes less than 1 (*e.g.* Vogel & Nussbaumer 1994), which confirms the complicated nature of the emission line region.

The Raman scattered features provide a special tool for investigation of the physical conditions of a symbiotic star through spectropolarimetry. Schmid & Schild (1994) provided spectropolarimetric data of some symbiotic systems, and more recently Harries & Howarth (1996) presented more data with enhanced resolution. The polarization behavior is also very heterogeneous and has complex structures. Schmid & Schild (1994) divided them into the three types and described the basic points. The extended ionized region may have definite effects on the polarization behavior displayed in the observational data as shown by Schmid (1996).

It has been pointed out by several researchers including Schmid (1996), and Harries & Howarth (1996,1997) that the position angle varies throughout the Raman scattered features. This implies that the most general model should include those producing the polarization direction other than the binary axis. Because the polarization behavior based on the models possessing a symmetry with respect to the binary axis does not show any rotation of the position angle, it has been proposed to consider non-spherical models.

Harries & Howarth (1996) pointed out that most of the Raman scattered features show multiple peak structures in the flux and in the polarized flux, and in particular double and triple peaks are found very frequently. These structures are maybe coupled with the complicated profiles of the UV emission lines including a P-Cygni type profile. If the incident UV line profile has a double-peaked structure, the similar structure is obtained in the scattered profile and in the polarized flux. However, the location of the peaks may differ depending sensitively on the wind terminal velocity. In this regard, it is necessary to consider various input profiles for reproducing the characteristics of the observed Raman scattered fluxes.

Some fraction of symbiotic stars show polarization flip around the red wing of the scattered features, which is produced in the Monte Carlo computation when the orbital

motion of the hot component about the cool giant is included. Typical parameters of symbiotic stars imply that the rotation velocity is almost comparable to the wind terminal velocity (*e.g.* Eq. (4.6)), and the polarization flip is shown clearly when the orbital plane coincides with the sky plane. The orbital motion can be observed by a careful monitoring of the position angle variation (*e.g.* Schild & Schmid 1996). However, we predict that the polarization flip will be seen irrelevant of the orbital phase, because the inclination angle of the orbital plane with respect to the line of sight does not change with the orbital motion,

Furthermore, the polarization flip is shown in the blue part when the orbital velocity exceeds the wind terminal velocity. In this case, the polarized flux shows a clear triple-peaked structure. Therefore, an independent observational determination of the orbital velocity will provide a good constraint to the wind terminal velocity, which is proportional to the mass loss rate of the cool giant.

It is proposed that the effect of the binary motion may leave an important signature in the polarization and polarized flux. It will be also interesting to investigate the combined effects of the binary motion and the non-Gaussian input profiles with different ionization structures. However, the introduction of the binary motion breaks the azimuthal symmetry and requires a good amount of computation time and a huge volume of parameter space to be examined. Therefore, independent determination of the kinematic and the dynamic parameters by the UV observations and monitoring of spectropolarimetry are expected to unveil the physical nature of symbiotic stars.

7. Summary

The Raman scattered features are quite unique to symbiotic stars so far and can be used as a powerful diagnostic of the physical conditions including the ionization structures and the kinematics on the orbital motion and the stellar wind structures. They possess several distinguished characteristics. The first and the most important point is that they are usually strongly polarized and therefore spectropolarimetry reveals a significant amount of information about the kinematics and the scattering geometry. Related with this is that they are composed of purely scattered photons without dilution from the direct flux retaining the vivid information on the scattering geometry. The third point is that the inelastic nature of the Raman process provides the enhancement of the profile width by a factor of λ_f/λ_i , which amounts to almost an order of magnitude in the case of the O VI doublets.

In this study, we reproduce the general properties of the Raman scattered emission lines, which are found in the works of many researchers including Schmid (1995, 1996) and Harries & Howarth (1997). The spherical wind model usually gives a large degree of polarization in the blue wing and the polarization flip around the center of the feature depending on the scattering optical depth.

If we take the orbital motion of the hot component around the cool giant into consideration, then the polarization flip is seen to shift to the red wing when the orbital plane is near to the sky plane. This effect is conspicuously seen when the orbital velocity is almost comparable to the terminal velocity of the stellar wind, giving insight into the spectropolarimetric data of several symbiotic stars including RR Tel (*e.g.* Espey et al. 1995, Harries & Howarth 1996, Schmid 1996). When the orbital velocity exceeds greatly the terminal

velocity, the polarization flip is expected to occur both in the blue wing and in the red wing. We also expect that various input profiles proposed by generic dynamical models can be combined to produce the complex features in the Raman scattered lines.

Much parameter space remains to be investigated by numerical methods, including the parameters \dot{M} , β , X_H , v_∞ , v_{rev} to list a few, and it is hoped that the numerical calculation may provide a useful constraint to existing dynamical models. It is generally concluded that spectropolarimetry will remain a useful tool to delve into the symbiotic system.

Acknowledgements

We are grateful to Profs. M. G. Lee, S. S. Hong for helpful discussions. We are also grateful for the valuable comments by the referee, Dr. H. Schmid. H. W. L gratefully acknowledges the support from the Research Institute for Basic Sciences at the Seoul National University. K. W. L was supported in part by KOSEF directed research grant 94-0702-04-01-3 and KOSEF non-directed research grant 971-0203-013-2.

REFERENCES

- Allen D. A., 1980, MNRAS, 190, 75
- Berestetskii V.B., Lifshitz E.M., Pitaevskii L.P., 1971, Relativistic Quantum Mechanics.
Pergamon Press, New York
- Espey B. R. et al. , 1995, ApJ, 454, L61
- Harries T.J., Howarth I.D., 1996, A&AS, 119, 61
- Harries T.J., Howarth I.D., 1997, A&AS, 121, 15
- Iben Jr. I., Tutukov A. V., 1996, ApJS, 105, 145
- Islaker H., Nussbaumer H. Vogel M., 1989, A&A, 219, 271
- Lee H. W., Blandford R. D. Western R., 1994, MNRAS, 267, 303
- Lee H. W., Lee K. W., 1996, Journal of Korean Astronomical Society Supplement, 29,
S249
- Lee H. W., Lee K. W., 1997, MNRAS, 287, 211 (Paper I)
- Mueller B. E. A., Nussbaumer H., 1985, A&A, 145, 144
- Nussbaumer H., Vogel M., 1987, A&A, 182, 51
- Osterbrock D. E., 1970, ApJ, 159, 823
- Pereira C. B., Vogel M., Nussbaumer H., 1995, A&A, 293, 783
- Schmid H. M., 1989, A&A, 211, L31
- Schmid H. M., 1992, A&A, 254, 224
- Schmid H. M., 1995, MNRAS, 275, 227
- Schmid H. M., 1996, MNRAS, 282, 511
- Schmid H. M., Schild H., 1990, A&A, 236, L13
- Schmid H. M., Schild H., 1994, A&A, 281, 145
- Schild H., Schmid H. M., 1996, A&A, 310, 211
- Seaquist E. R., Taylor A. R., Button S., 1984, ApJ, 284, 202
- Vogel M., Nussbaumer H., 1994, A&A, 284, 145

FIGURE CAPTION

Figure 1.- A schematic geometry of a symbiotic star system for the Monte Carlo calculation. The z -axis is chosen to be the binary axis and the observer's line of sight coincides with x -axis. The hot star is represented by the circle on the right side, and the bigger circle in the origin is the cool giant. A spherically symmetric stellar wind is shown by radial (small) arrows. The vectors $\vec{\rho}_i$ and $\vec{\rho}_{i+1}$ represent the i -th and the $i+1$ -th scattering sites respectively and $s(\tau_i)$ is the spatial distance between the two scattering sites. b is the impact parameter of the photon trajectory with respect to the cool giant.

Figure 2.- A contour map of the Doppler factors and the scattering optical depths of incident photons from the hot star. The stellar wind is a spherical one defined in section 2.2. The Doppler factor is defined by $DF \equiv \hat{\mathbf{k}}_i \cdot \mathbf{v}/c$ and the total scattering optical depth $\tau_s \equiv \int ds n(s)(\sigma_{Ray} + \sigma_{Ram})$. The adopted parameters are described in Paper I.

Figure 3.- Comparison of the single scattering approximation with corresponding Monte Carlo calculation. The dotted lines represent the Monte Carlo result and the result from the single scattering approximation is shown by the solid lines.

Figure 4.- The Rayleigh and Raman reflected fluxes from a finite slab of total scattering optical depth $\tau_s = 0.5, 1, 5, 10$ as a function of the number of scattering. The light lines represent the result for the case $R_{Ray} = 0.2$ and the case for $R_{Ray} = 0.8$ is shown by the thick lines. The solid lines are for the Raman scattered flux and the dotted lines are for the Rayleigh case.

Figure 5.- The Rayleigh and the Raman reflected fluxes from a slab of the total scattering optical depth $\tau_s = 10$, $R_{Ray} = 0.8$ as in Fig. 4(d) with semi-quantitatively described $f_{Ram}(n)$, $f_{Ray}(n)$ in section 3.2. The solid lines are for the Monte Carlo results, and the dotted lines give $f_{Ram}(n)$, $f_{Ray}(n)$ computed using Eqs. (3.3)-(3.6). The upper set of curves are Raman scattered lines and the lower set corresponds to the Rayleigh flux. In the bottom panel, $f_{Ram}(n)$, and $f_{Ray}(n)$ calculated from a different escape probability $\beta'(n) = \exp(-n^{0.4})/2$ (Eq. (3.7)).

Figure 6.- The line profiles and the polarization for the simple Gaussian case, where the UV emission line profiles are described by a Gaussian with $T_{em} = 10^4$ K. See the text for more detail.

Figure 7.- A typical ionization structure around the hot star of a symbiotic system, reproduced using the recipes provided by Seaquist et al. (1984). The parameter X_H defined in Eq. 4.2 determines the overall structure of the ionized region. Solid lines divide H I region for H II. Dotted lines are obtained using a simpler equation for the ionization front.

Figure 8.- Monte Carlo results corresponding to the ionization structures described in Fig. 7.

Figure 9.- Monte Carlo results for the disk-wind models.

- (a) The observer's line of sight lies in the equatorial plane of the disk wind and the typical scattering optical depths $\tau_0 = 0.5, 1.0, 10$.
- (b) The observer's line of sight is perpendicular to the equatorial plane.

Figure 10.- Monte Carlo results for the bipolar wind models.

- (a) The observer's line of sight is perpendicular both to the binary axis and to the wind symmetry axis and the scattering optical depths $\tau_0 = 0.5, 1, 10$.
- (b) The observer's line of sight coincides with the wind symmetry axis.

Figure 11.- Monte Carlo results for the cases where the input profiles are gives by single-peaked and double-peaked profiles. The input profiles are shown in a small box at upper right corner in each panel.

- (a) Single-peaked profile with $\tau_0 = 1$
- (b) Single-peaked profile with $\tau_0 = 10$
- (c) Double-peaked profile with $\tau_0 = 1$
- (b) Double-peaked profile with $\tau_0 = 10$

Figure 12.- Doppler- τ_s contours analogous to Fig. 2 including the relative motion of the hot component with respect to the cool giant. The hot star is assumed to move in $-y$ -direction with a velocity $v_{rev} = 0.6 v_\infty$, where v_∞ is the terminal velocity of the spherical stellar wind around the cool giant.

Figure 13.- Monte Carlo results corresponding to the case described in Fig. 12. The observer's line of sight is perpendicular to the orbital plane.

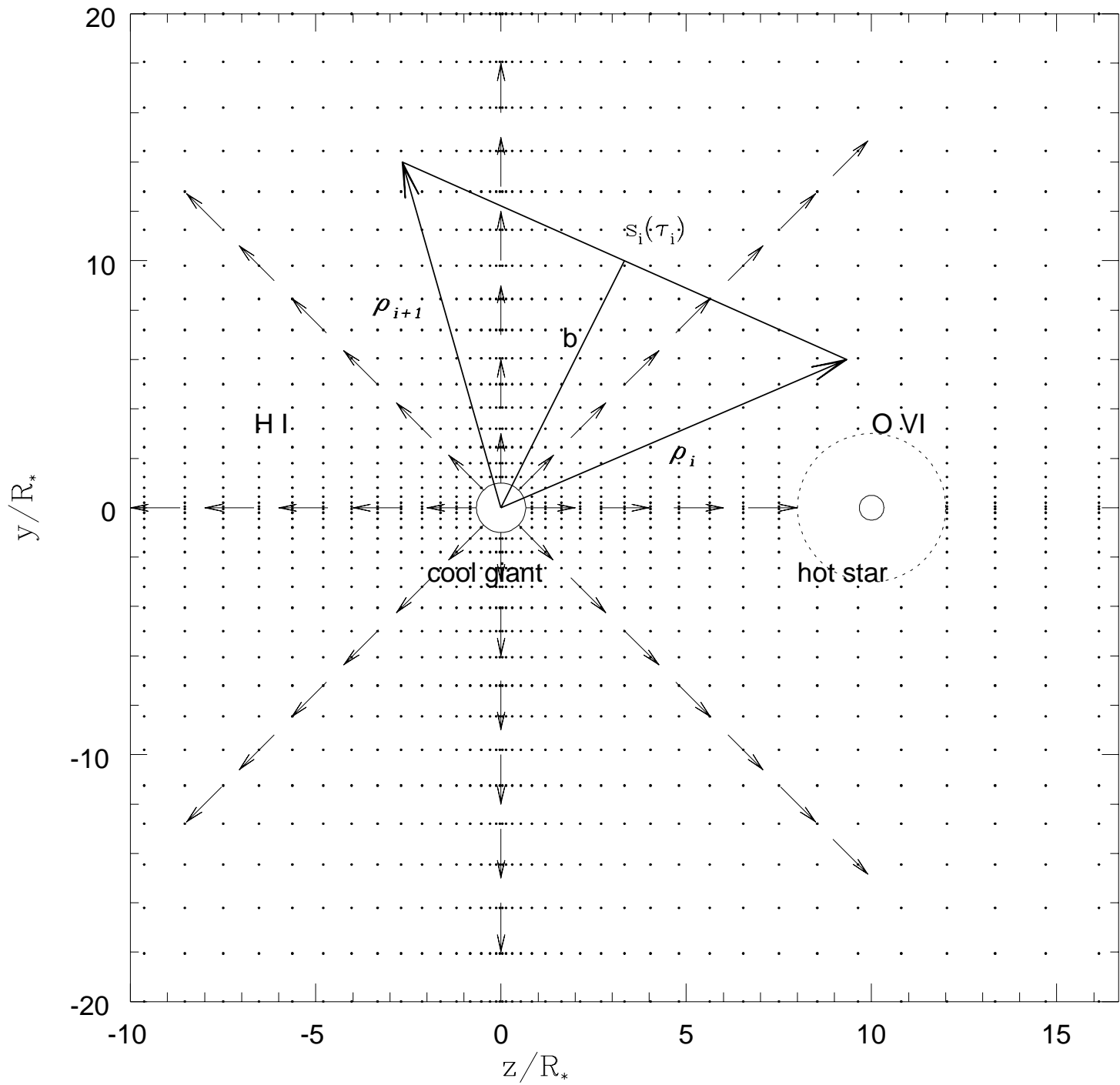
- (a) The typical scattering optical depth $\tau_0 = 1$
- (b) The typical scattering optical depth $\tau_0 = 5$

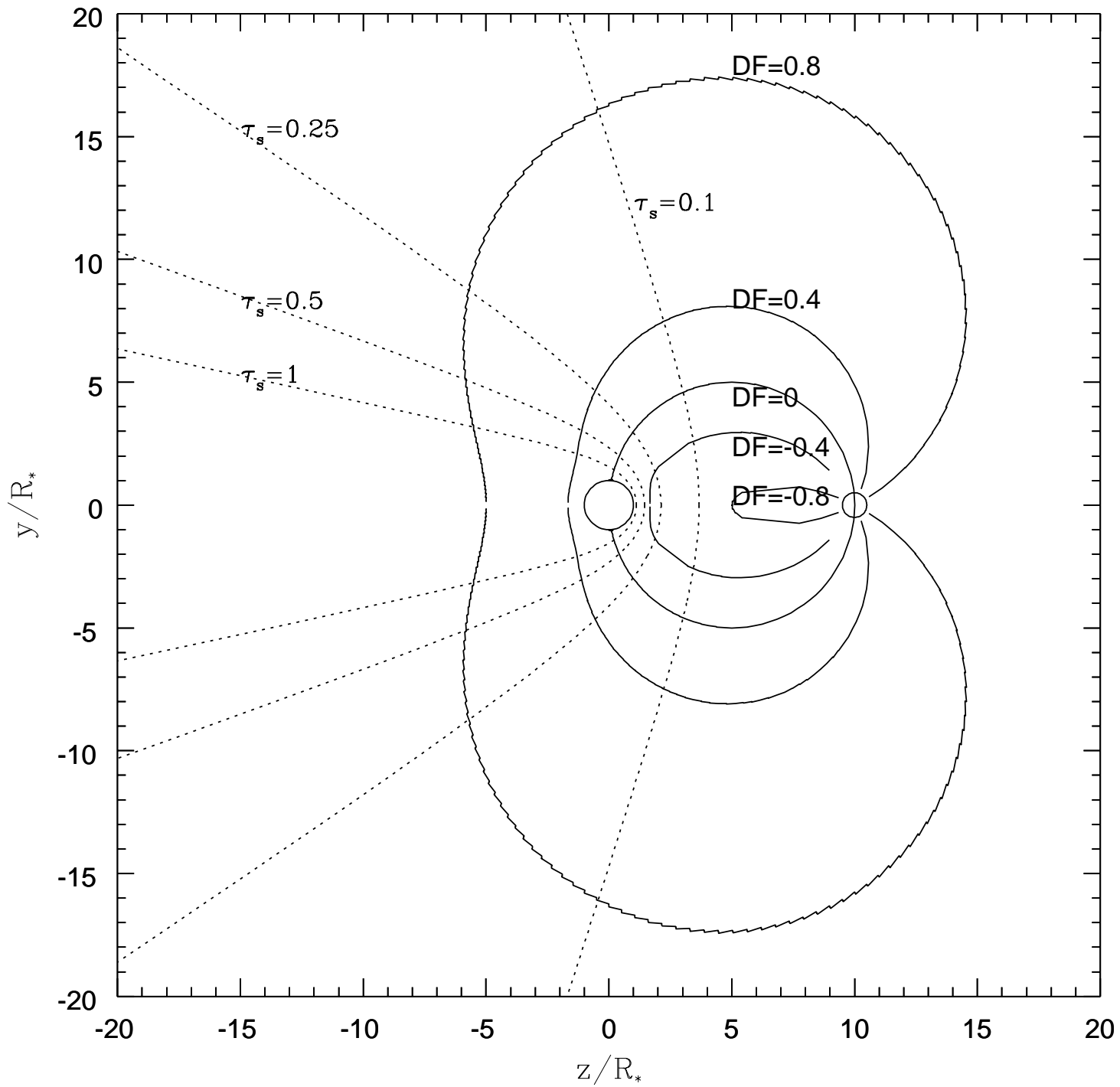
Figure 14.- Monte Carlo results for with $v_{rev} = 3 v_\infty$. The wind structure around the cool giant and the observer's line of sight are the same as in Fig. 12.

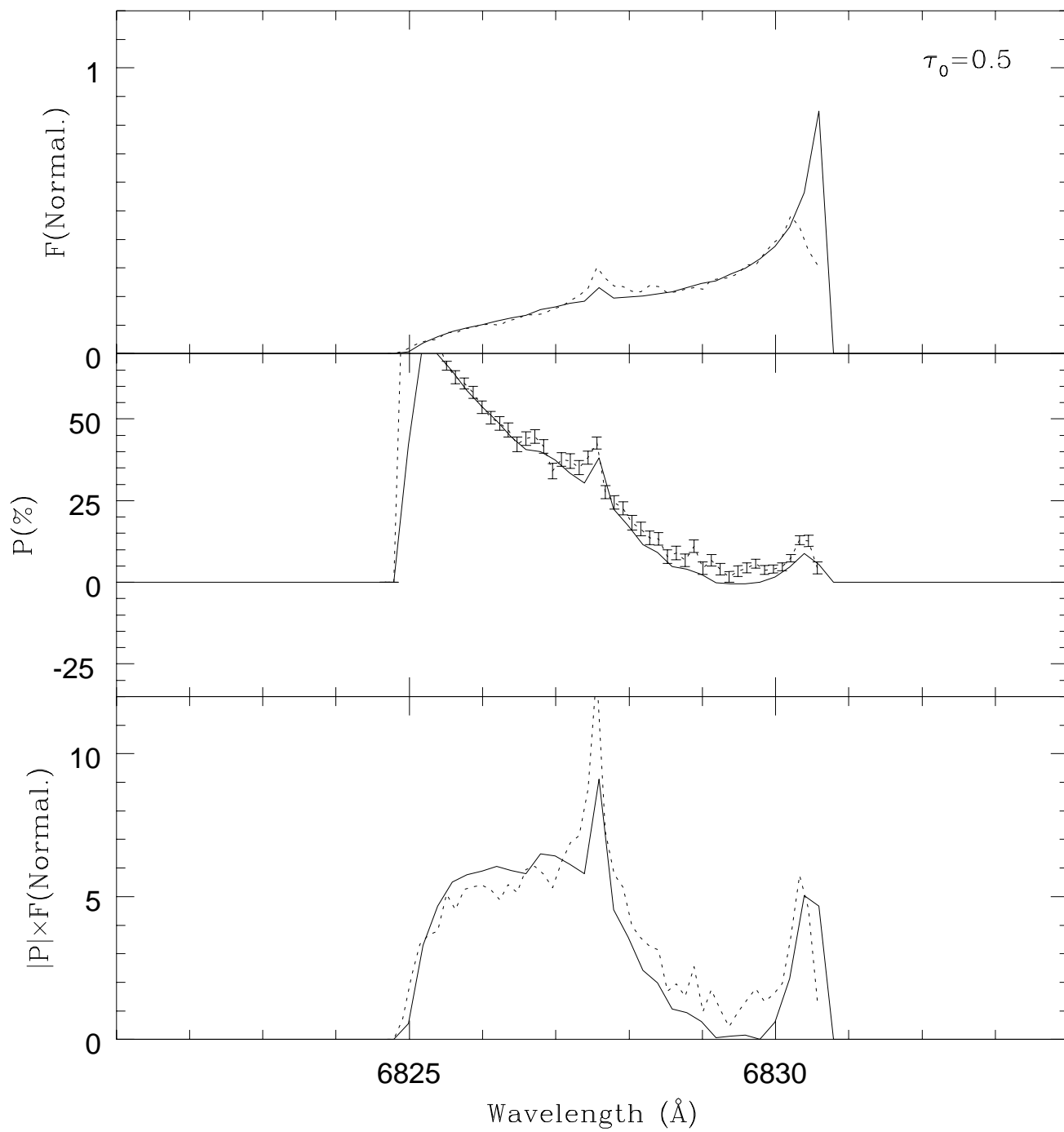
- (a) $\tau_0 = 1$, (b) $\tau_0 = 5$

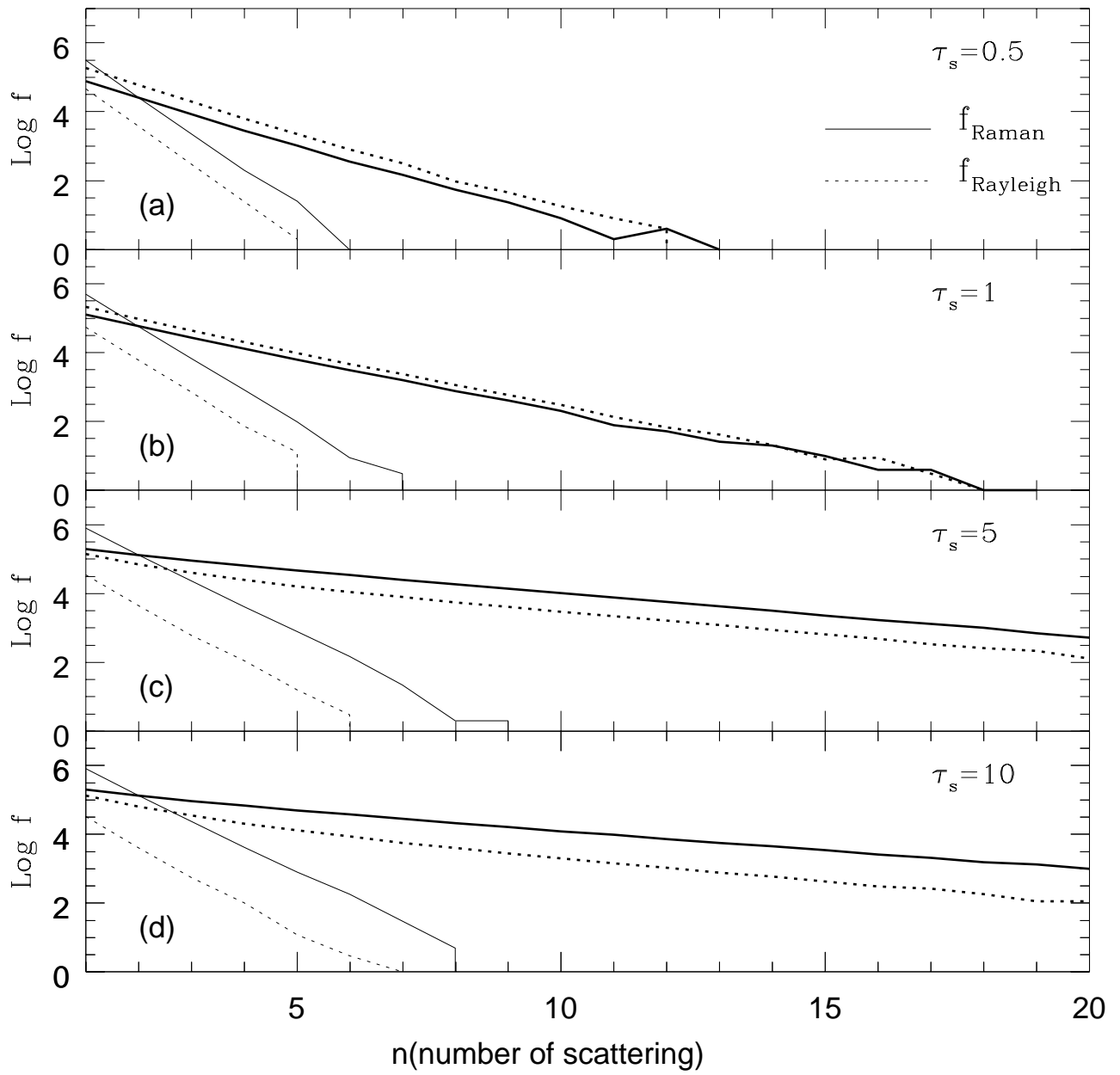
Figure 15.- Monte Carlo results for the same geometry with Fig. 12, where the observer's line of sight lies on the orbital plane.

- (a) $\tau_0 = 1$, (b) $\tau_0 = 5$









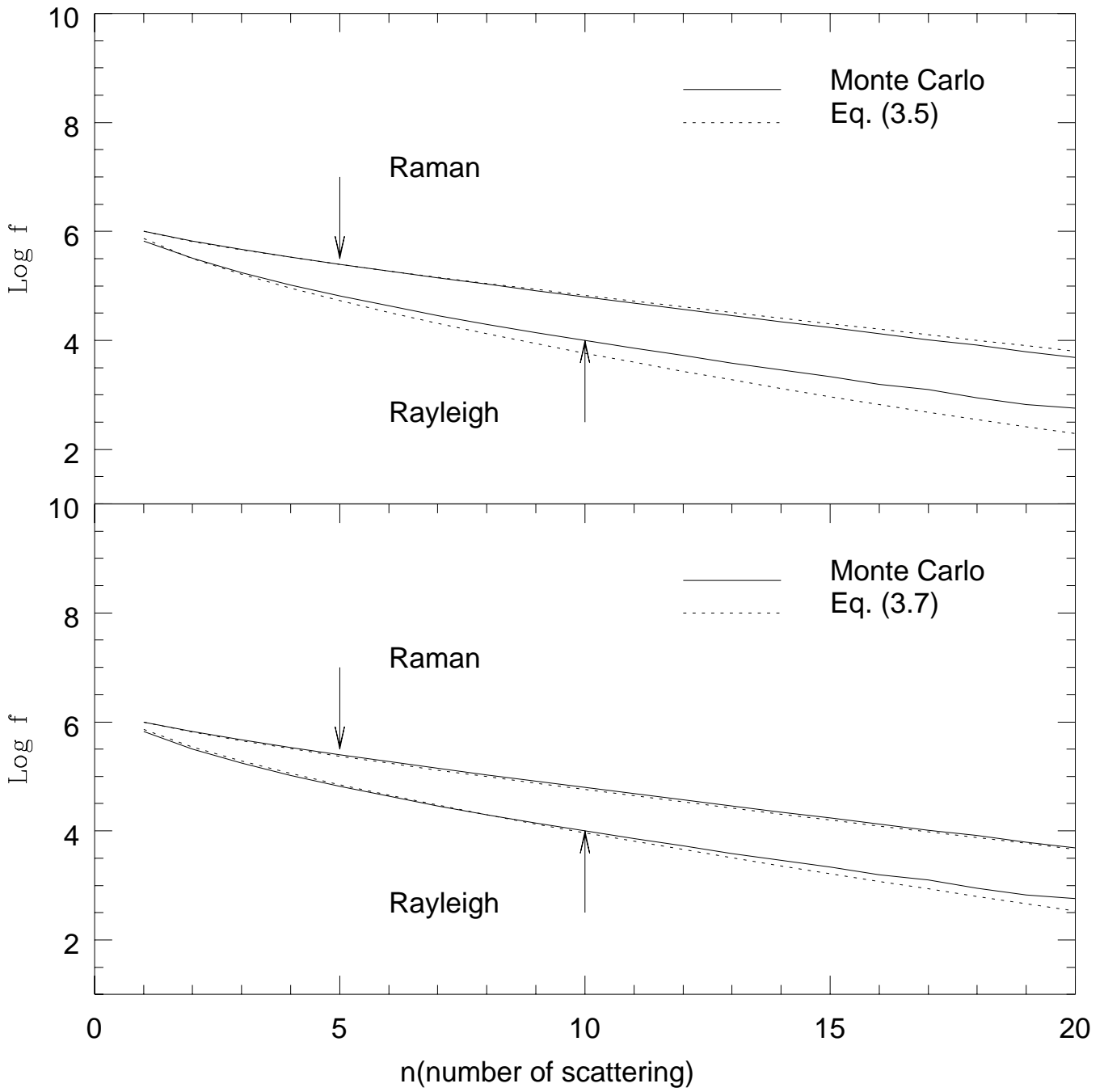
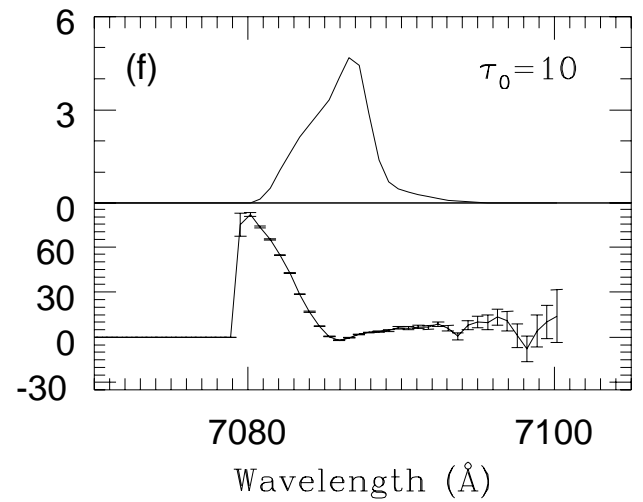
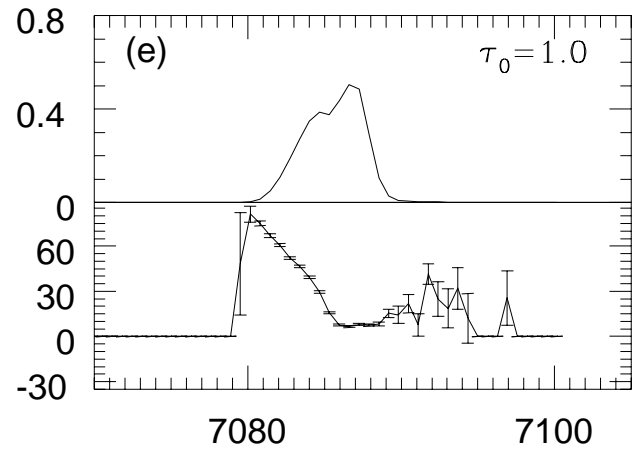
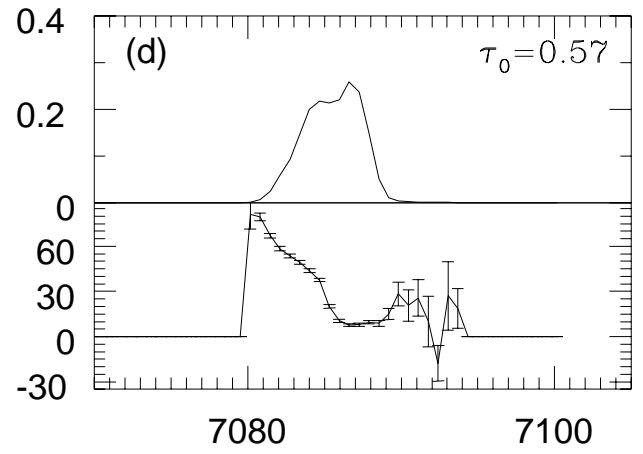
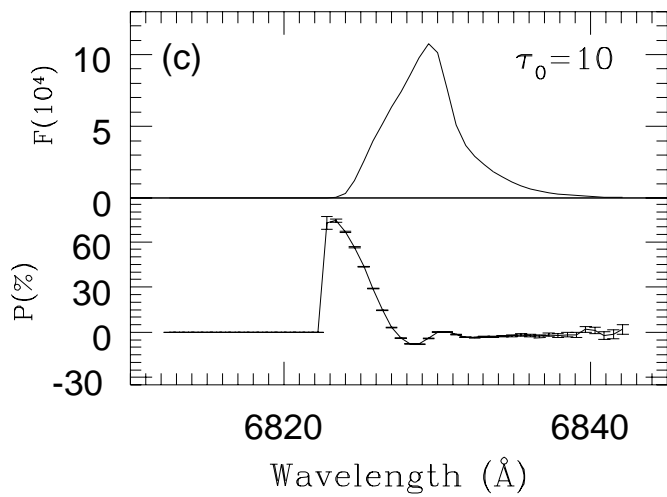
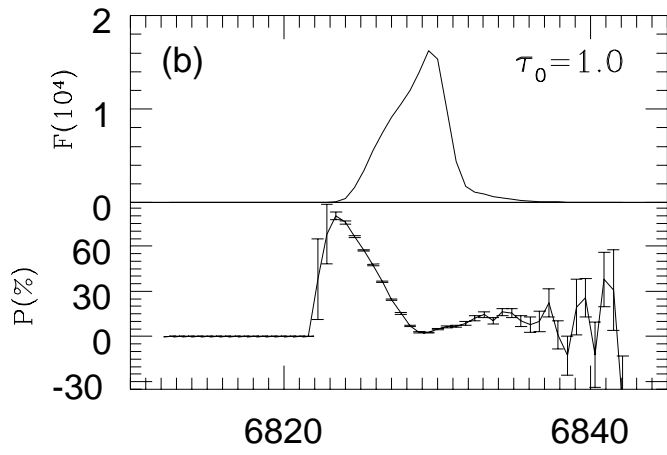
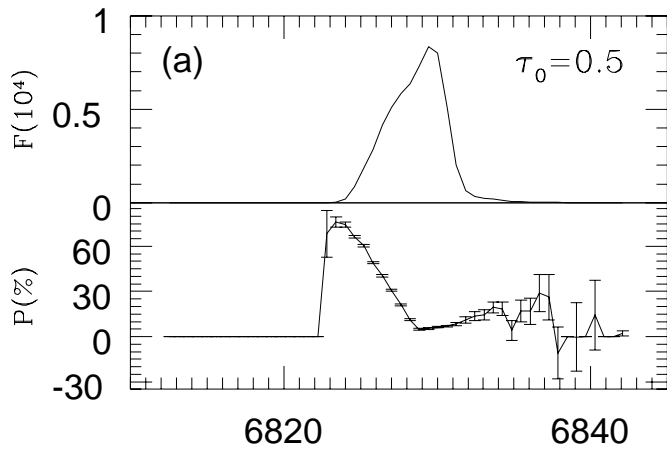
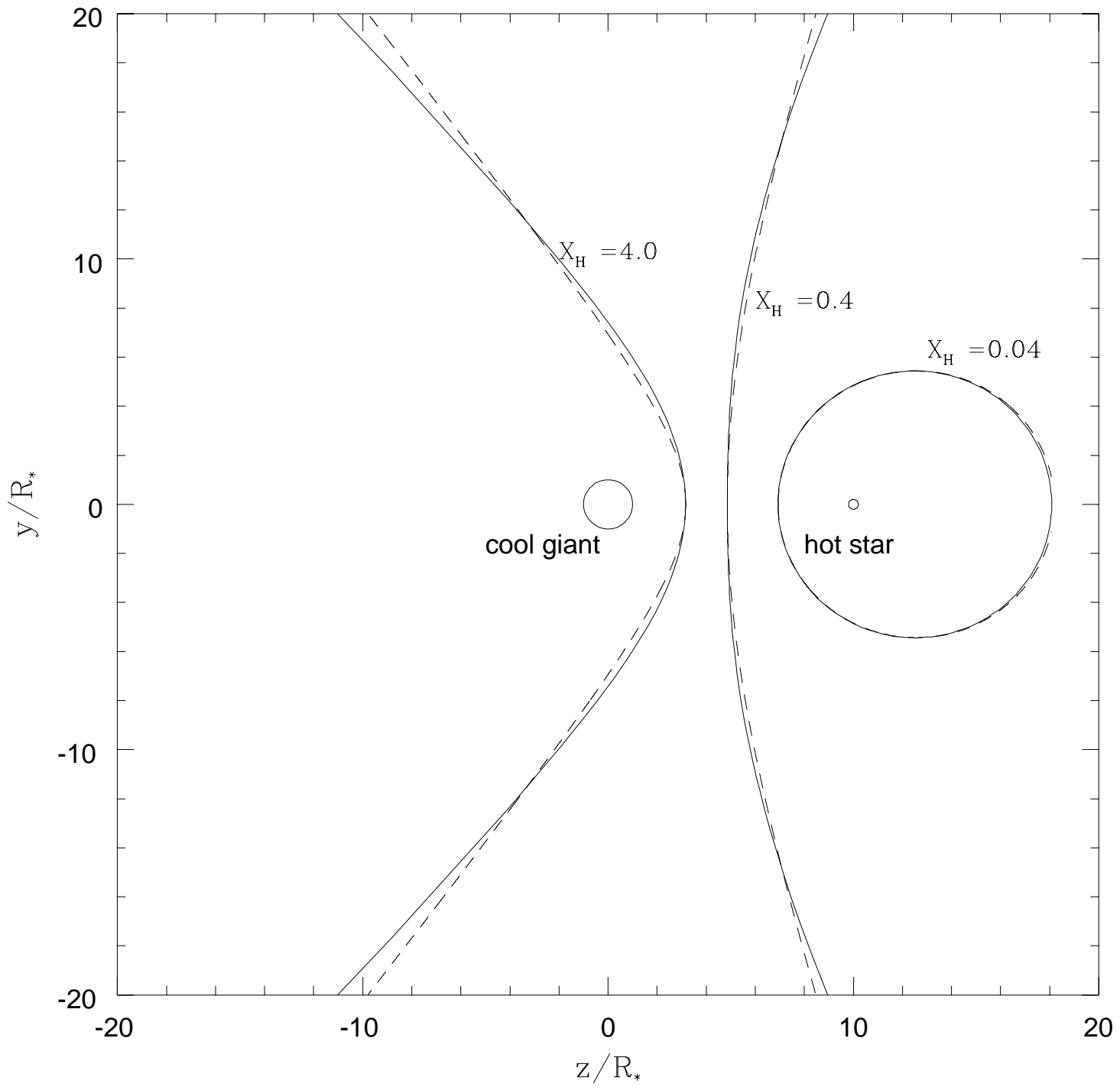
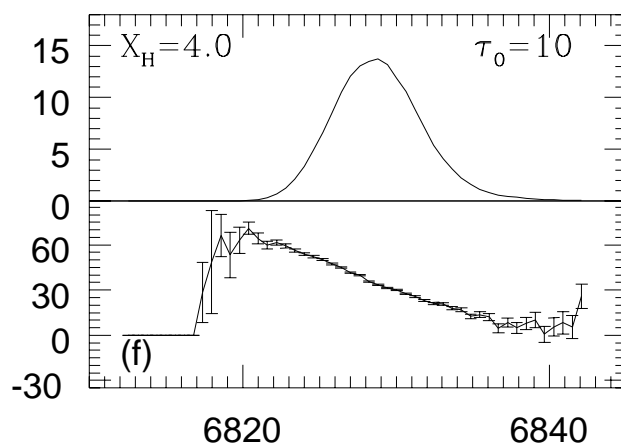
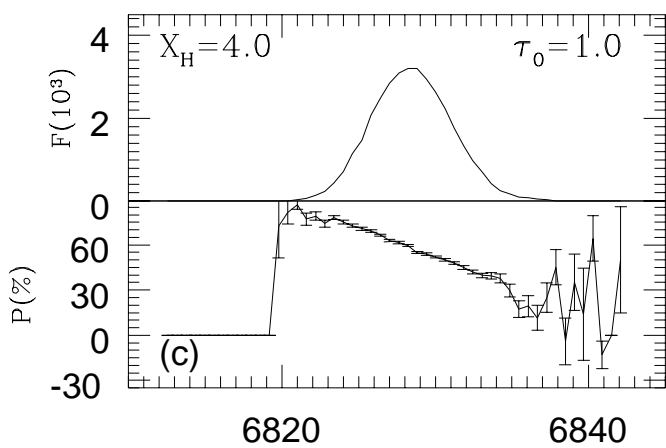
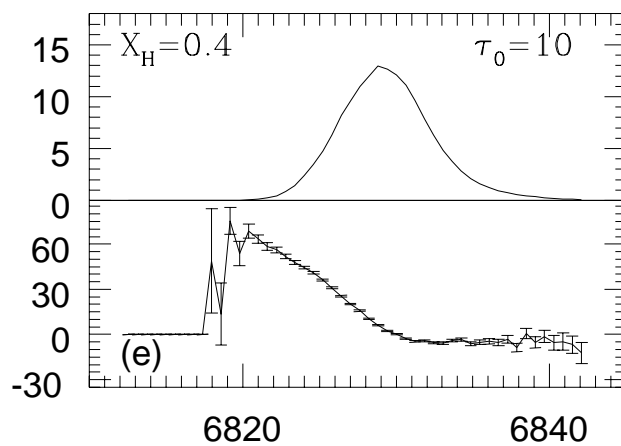
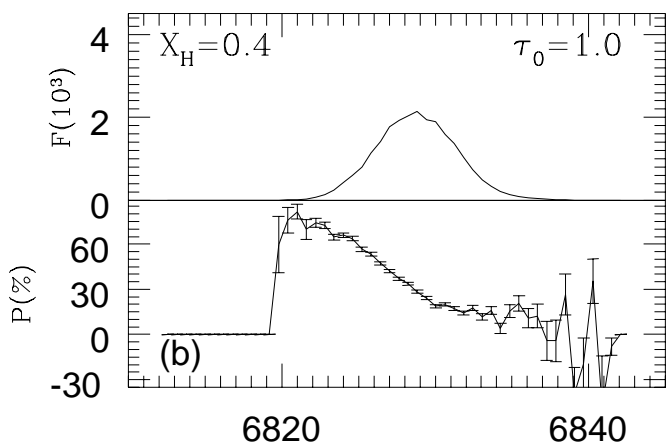
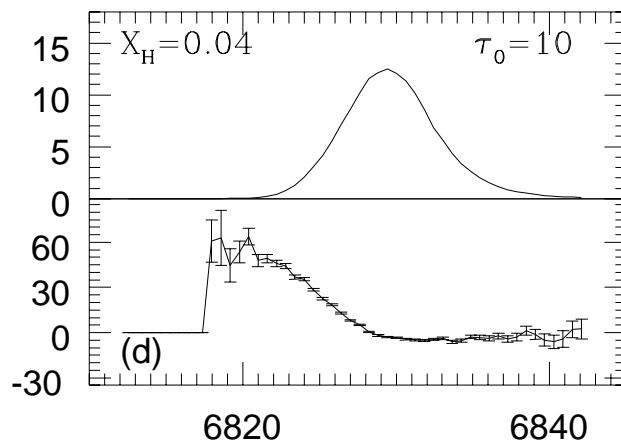
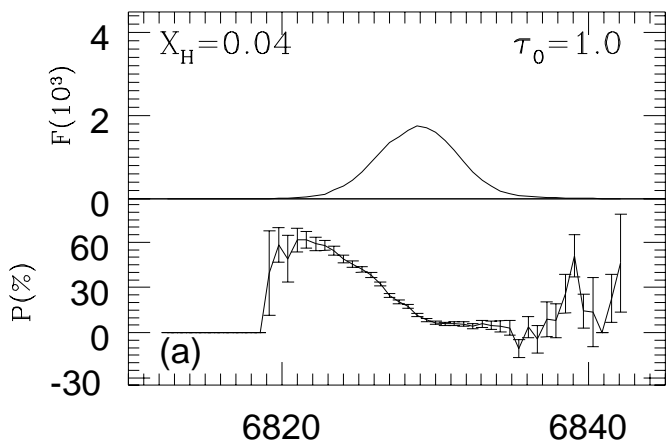


Fig 6



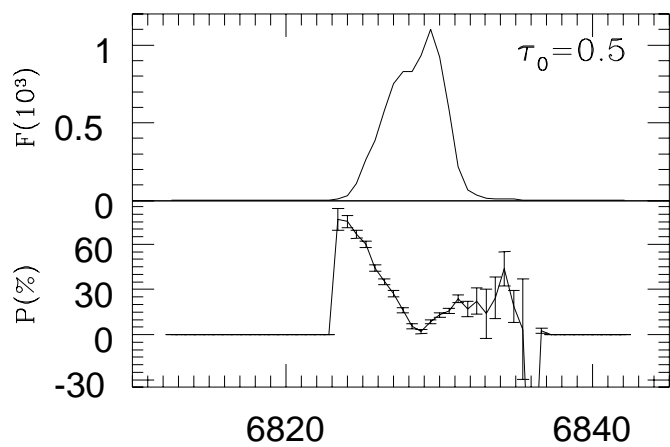




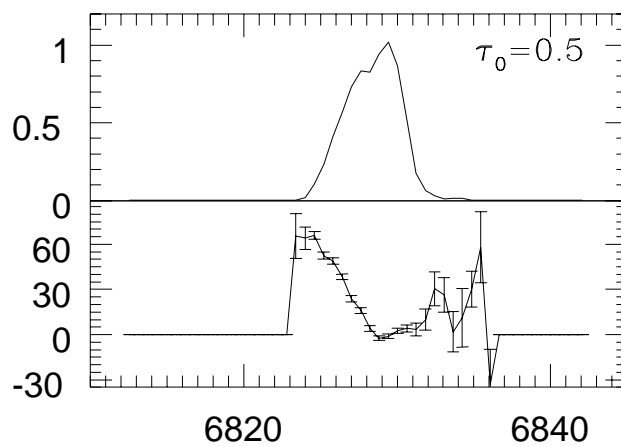
Wavelength (Å)

Wavelength (Å)

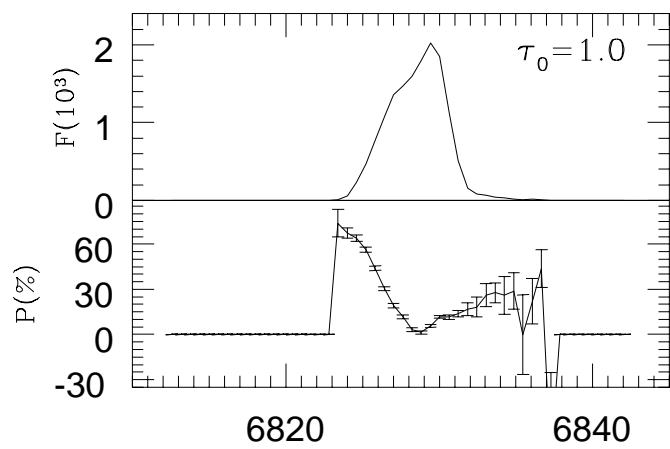
(a)



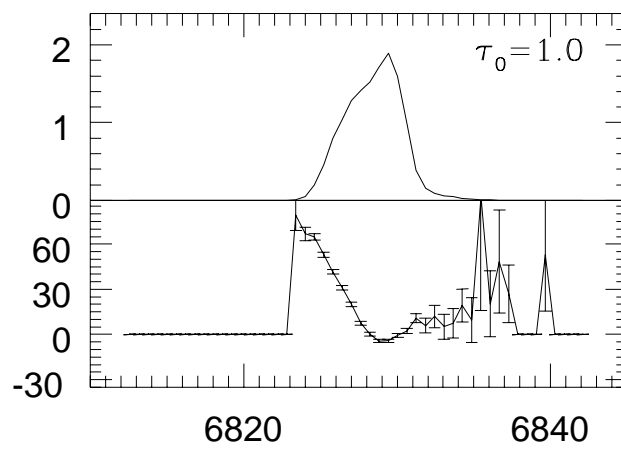
(b)



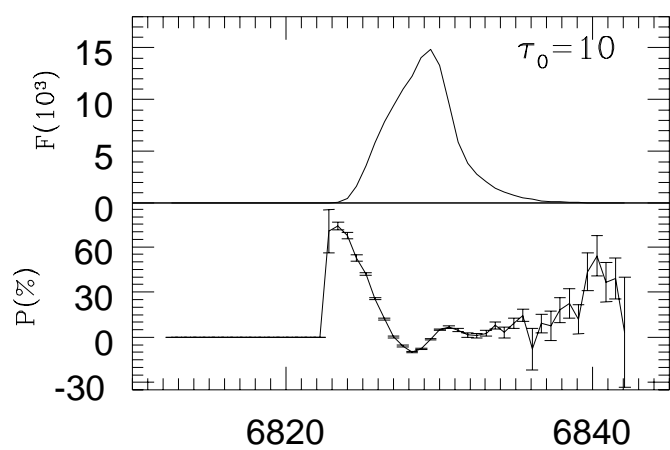
(a)



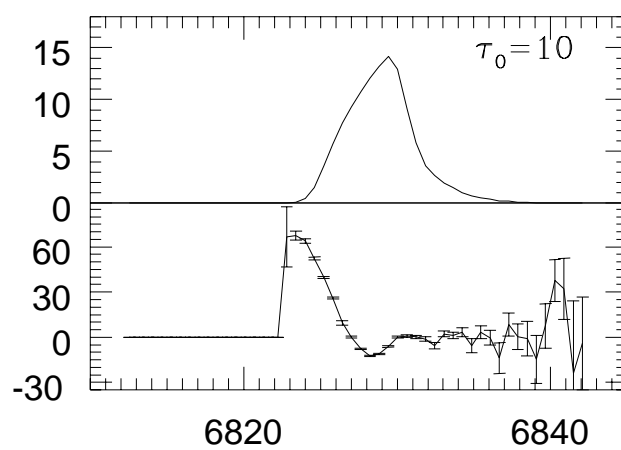
(b)



(a)



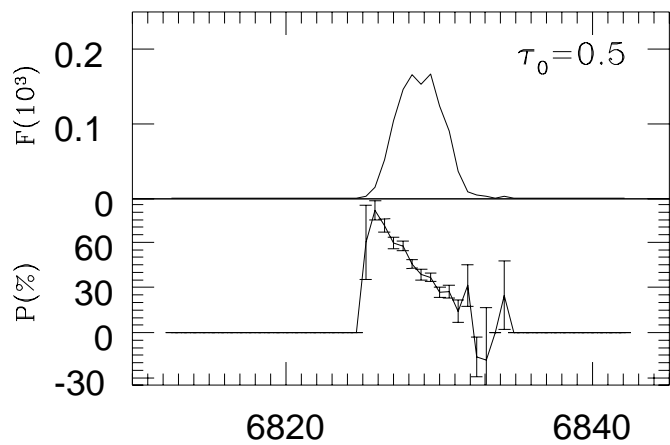
(b)



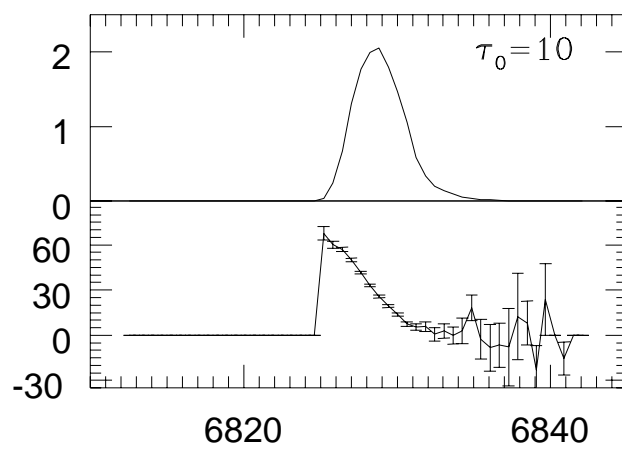
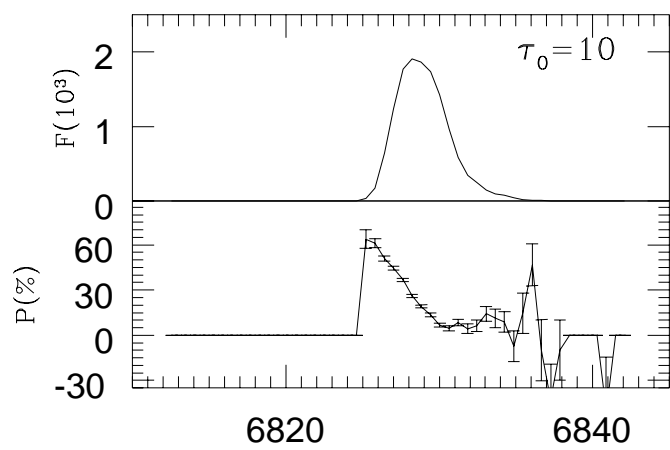
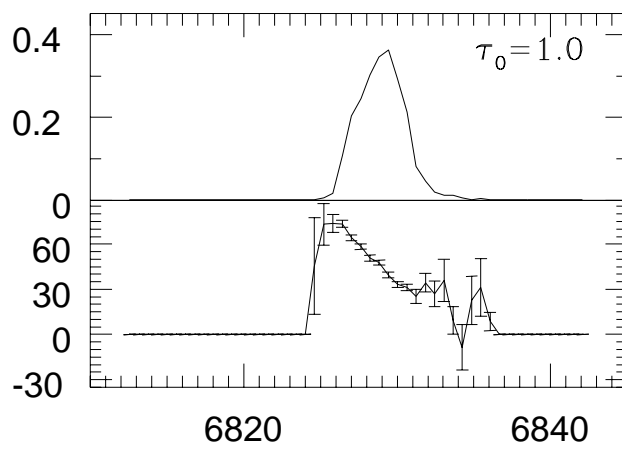
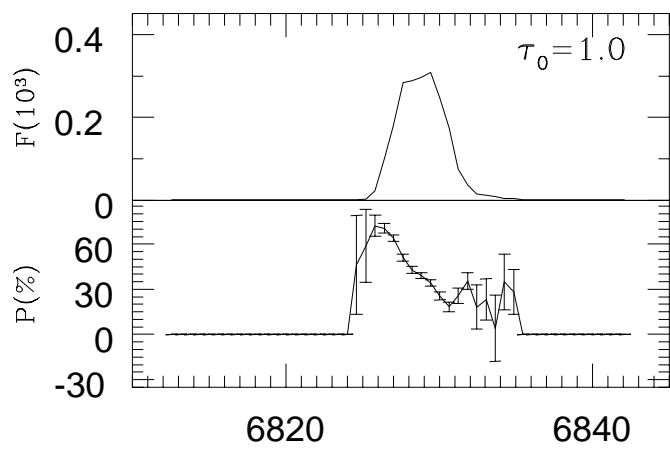
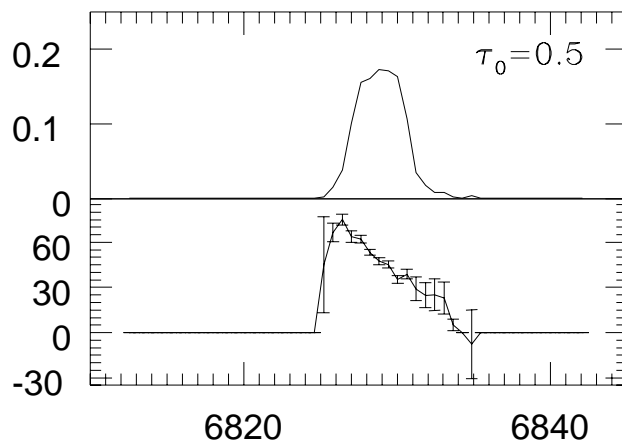
Wavelength (\AA)

Wavelength (\AA)

(a)



(b)



Wavelength (\AA)

Wavelength (\AA)

